Research in Astronomy and Astrophysics, 22:045003 (15pp), 2022 April https://doi.org/10.1088/1674-4527/ac4e01

A Study on White Dwarf Masses in Cataclysmic Variables Based on XMM-Newton and Suzaku Observations

Zhuo-Li Yu, Xiao-Jie Xu, and Xiang-Dong Li
School of Astronomy and Space Science and Key Laboratory of Modern Astronomy and Astrophysics, Nanjing University, Nanjing, 210093, China; xuxj@nju.edu.cn
Received 2021 December 9; revised 2022 January 16; accepted 2022 January 19; published 2022 March 17

Abstract

The distribution of the mass of white dwarfs (WDs) is one of the fundamental questions in the field of cataclysmic variables (CVs). In this work, we make a systematical investigation on the WD masses in two subclass of CVs: intermediate polars (IPs) and non-magnetic CVs in the solar vicinity based on the flux ratios of Fe XXVI–Lyα to Fe XXV–Heα emission lines ($I_{7.0}/I_{6.7}$) from archival XMM-Newton and Suzaku observations. We first verify the (semi-empirical) relations between $I_{7.0}/I_{6.7}$, the maximum emission temperature ($T_{\max}$) and the WD mass ($M_{\rm WD}$) with the mkcflow model based on the apec description and the latest AtomDB. We then introduce a new spectral model to measure $M_{\rm WD}$ directly based on the above relations. A comparison shows that the derived $M_{\rm WD}$ is consistent with dynamically measured ones. Finally, we obtain the average WD masses of 58 CVs (including 36 IPs and 22 non-magnetic CVs), which is the largest X-ray selected sample. The average WD masses are $\langle M_{\rm WD,IP}\rangle = 0.81 \pm 0.21\,M_{\odot}$ and $\langle M_{\rm WD,DN}\rangle = 0.81 \pm 0.21\,M_{\odot}$ for IPs and non-magnetic CVs, respectively. These results are consistent with previous works.

Key words: (stars:) binaries (including multiple): close – (stars:) novae – cataclysmic variables – X-rays: binaries

1. Introduction

A cataclysmic variable (CV) is a semi-detached binary where a white dwarf (WD) accretes gas from its main sequence or sub-giant companion star via Roche-lobe overflow. Subclasses of CVs include magnetic (mCVs, including polars and intermediate polars) and non-magnetic (non-mCVs, mostly dwarf novae) ones on terms of the magnetic field of WDs. In an intermediate polar (IP), the magnetic field is strong enough to truncate the accretion disk at a certain radius, and channel the accreted gas onto the magnetic poles of the WD along the magnetic lines. A standing shock is then formed above the surface of the WD. The post-shock gas is ionized and emits X-ray photons. For dwarf novae (DNe), the X-ray emission is supposed to be mainly from a boundary layer between the accretion disk and the surface of WD. The observed X-ray luminosities of IPs and DNe in quiescence are between 10^{30-34} erg s^{-1}. Their X-ray spectra can both be well described with an isobaric cooling flow model (mkcflow, e.g., see Mushotzky & Szymkowiak 1988), with a Gaussian component to describe the fluorescent Fe I–Kα line, and sometimes an additional partial absorption component which is suggested to originate from the un-shocked gas above the accretion column or in the accretion curtain (for a recent review of X-ray emission of CVs, see Mukai 2017).

The mass distribution of WDs in CVs is important not only for the theory of binary star evolution, but also for other interesting astrophysical objects. For example, massive WDs are closely related to the progenitors of Type Ia supernovae, which are supposed to be WDs reaching or near the Chandrasekhar mass limit. Based on the Ritter & Kolb (2003)'s CV catalog, Zorotovic et al. (2011) obtained a mean $M_{\rm WD} = 0.83 \pm 0.23\,M_{\odot}$ for solar vicinity CVs, which is $\sim$0.2–0.3 $M_{\odot}$ higher than the mean WD masses in single WDs (e.g., Kepler et al. 2007) and pre-CVs (Zorotovic et al. 2011). Moreover, the mean WD masses in CVs in the Galactic bulge and Galactic center were determined as $\sim$0.8 $M_{\odot}$ (Yu et al. 2018) and $\sim$0.9 $M_{\odot}$ (Hailey et al. 2016), which are again $\sim$0.2–0.3 $M_{\odot}$ higher than single WDs and pre-CVs. The physical scenario responsible for the differences has not been fully understood (e.g., Knigge 2006; Knigge et al. 2011).

The WD mass distribution in CVs is worth revisiting. First, the CV sample in Zorotovic et al. (2011) was directly taken from Ritter & Kolb (2003)'s catalog, in which the WD masses were measured with various methods by various authors, so the reliability of the measured masses might be a problem. Second, Zorotovic et al. (2011) had to manually select a sample of 32 "fiducial" CVs (those with high quality measurements) from a whole sample of 104 sources, thus the sample may include some bias. With X-ray spectroscopy, it is now possible to make a systematic survey on WD masses in CVs in the solar vicinity. The results would surely provide helpful clues to improve our understanding on this topic.

Traditionally, the WD mass in a CV is measured by the dynamical method (e.g., eclipse light curves, radial velocity curves, etc), but the results are suffered from uncertainties, e.g., inclination angles. Since the last decades, X-ray spectroscopy has provided an alternative way to measure WD masses in IPs with the $T_{\rm max}$–$M_{\rm WD}$ relation. In an IP, the WD mass is related to $T_{\rm max}$ in strong shock condition (assuming the accreted gas falls from infinity) with the following equation (Frank et al. 2002):

$$T_{\rm max} = \frac{3}{8}\frac{\mu m_{\rm H}}{k}\frac{GM_{\rm WD}}{R_{\rm WD}}, \tag{1}$$

where μ, $m_{\rm H}$, k, G, $M_{\rm WD}$ and $R_{\rm WD}$ are the mean molecular weight, the mass of H atom, the Boltzmann constant, the gravitational constant, the WD mass and the WD radius, respectively. Combining Equation (1) with $T_{\rm max}$ measured from the hard (up to 30–50 keV) X-ray continua, and the $M_{\rm WD}$–$R_{\rm WD}$ relation (e.g., Nauenberg 1972), various authors have measured $M_{\rm WD}$ in IPs in the solar vicinity (e.g., Yuasa et al. 2010; Shaw et al. 2018; Yu et al. 2018; Suleimanov et al. 2019; Shaw et al. 2020). Yuasa et al. (2010) and Bernardini et al. (2012) further derived the mean $M_{\rm WD}$ values in IPs to be $0.88 \pm 0.25\,M_\odot$ and $0.86 \pm 0.07\,M_\odot$, respectively. Similarly, Suleimanov et al. (2019) derived an average $M_{\rm WD} = 0.79 \pm 0.16\,M_\odot$ for a sample of 35 IPs observed by NuSTAR and Swift/BAT.

For DNe, there is currently no widely accepted theory on the physics of boundary layer. The accreted gas may be heated either by a strong shock or a series of weak shocks in the boundary layer (Frank et al. 2002). Thus, there is no well-defined equations like Equation (1). Recently, Yu et al. (2018) obtained a semi-empirical relation between $T_{\rm max}$ and $M_{\rm WD}$ for DNe from X-ray observations of solar vicinity DNe:

$$T_{\rm max} = \alpha\frac{3}{16}\frac{\mu m_{\rm H}}{k}\frac{GM_{\rm WD}}{R_{\rm WD}}, \tag{2}$$

where $\alpha = 0.646 \pm 0.069$ (for comparison, $\alpha = 1$ under the strong shock assumption).

The hard X-ray continuum method requires spectra with good counting statistics up to 30–50 keV to obtain reliable measurements of $T_{\rm max}$ and $M_{\rm WD}$. However, the small effective area and/or the high background level of current X-ray telescopes usually lead to low quality hard X-ray spectra. Moreover, the complex, un-modeled intrinsic absorption found in some IPs, and the existence of the X-ray reflection (Mukai 2017; Shaw et al. 2018, 2020) may also lead to deviated $T_{\rm max}$, thus biased WD masses.

The flux ratio of Fe XXVI–Lyα to Fe XXV–Heα lines ($I_{7.0}/I_{6.7}$) has been suggested as a good diagnostic for $T_{\rm max}$, and thus $M_{\rm WD}$ in CVs (e.g., Ezuka & Ishida 1999; Xu et al. 2019b). The basic idea is that more helium-like iron ions will be ionized to hydrogen-like ones in higher plasma temperatures, resulting to higher iron flux ratios. The advantage of this line ratio method is that present X-ray telescopes like XMM-Newton and Chandra (and Suzaku which stopped working in 2015) have better energy resolution and larger effective area near the iron line (6–7 keV) compared to 30–50 keV hard X-ray energy ranges, enabling reliable $I_{7.0}/I_{6.7}$ measurements. Additionally, instruments which are sensitive in this energy range include XMM-Newton and Chandra, which have good angular resolution, so that individual sources in the Globular cluster and toward the Galactic bulge/center direction could be resolved and investigated (e.g., Zhu et al. 2018; Xu et al. 2019a). Moreover, the flux ratio of Fe lines is less affected by intrinsic absorption and reflections. Early work by Ezuka & Ishida (1999) measured the $I_{7.0}/I_{6.7}$ values of solar vicinity CVs to derive $M_{\rm WD}$ in IPs based on ASCA observations. Recently, Xu et al. (2016) and Yu et al. (2018) suggested the $T_{\rm max}$–$I_{7.0}/I_{6.7}$–$M_{\rm WD}$ relations for IPs and DNe based on Suzaku observations of solar vicinity CVs, and obtained a mean WD mass of $0.81 \pm 0.07\,M_\odot$ for CVs in the Galactic Bulge. Xu et al. (2019b) further suggested that $I_{7.0}/I_{6.7}$ can be used as a good diagnostic of WD mass in IPs and DNe based on Suzaku and NuSTAR observations, and suggested the existence of massive ($\sim$1.0–1.2 $M_\odot$) WDs in CVs in the Galactic center region (Xu et al. 2019a).

It is now possible to derive the mass of WDs in CVs, especially those in non-magnetic ones in the solar vicinity based on the $T_{\rm max}$–$I_{7.0}/I_{6.7}$–$M_{\rm WD}$ relations. Before that, a thorough examination on these relations with the new atomic database must be made, because the results in previous works were based on the cooling flow model (mkcflow in Xspec) with the older mekal (and thus the old atomic database) emission description. Moreover, the $T_{\rm max}$–$I_{7.0}/I_{6.7}$–$M_{\rm WD}$ relations could be built into the mkcflow model, so that the spectral fitting can output $M_{\rm WD}$ directly, and save the trouble of comparing the fitted $T_{\rm max}$ or $I_{7.0}/I_{6.7}$ with the $T_{\rm max}$–$M_{\rm WD}$ and $I_{7.0}/I_{6.7}$–$M_{\rm WD}$ curves to derive $M_{\rm WD}$.

In this work, we utilize the archival XMM-Newton and Suzaku observations of 58 individual CVs, including 36 IPs and 22 non-mCVs in the solar vicinity to investigate their WD masses. We start by examining the $I_{7.0}/I_{6.7}$–$M_{\rm WD}$ relations with the cooling flow model with apec emission description based on the AtomDB. We then introduce a new spectral model with built-in $T_{\rm max}$–$I_{7.0}/I_{6.7}$–$M_{\rm WD}$ relations to directly output WD masses. We further assess $M_{\rm WD}$ from both XMM-Newton and Suzaku observations and obtain the mean $M_{\rm WD}$ of the sampled CVs. Additionally, mCVs and non-mCVs follow the similar distribution of WD mass in the standard CV evolutionary model (Zorotovic & Schreiber 2020), but the formation of high magnetic field WDs were suggested to be related to the common envelope evolution (e.g., Briggs et al. 2018), which may lead to a different WD masses between mCVs and non-mCVs. In this work, we will explore the mean WD mass of IPs and non-mCVs and check whether they are consistent with each other.

The rest of this paper is organized as follows. In Section 2, we introduce the sample selection and data preparation, and measure their $I_{7.0}/I_{6.7}$. In Section 3, we update the $T_{\rm max}$–$M_{\rm WD}$ relation of DNe and introduce a new spectral model to measure the WD masses, with which the $M_{\rm WD}$ of sampled CVs are derived. We make a brief discussion in Section 4 and summarize in Section 5. All results measured in this work are shown at 90% confidence level. On the other hand, the dynamically measured masses in CVs are directly taken from the references with 68% confidence level.

2. Observations and Data Analysis

XMM-Newton is chosen as the main instrument in this work because it provides the most observations of CVs in the solar vicinity compared to other X-ray instruments. The XMM-Newton observatory contains three X-ray instruments and one Optical Monitor to provide simultaneous X-ray and optical/UV observations. The three X-ray instruments are: European Photon Imaging Camera Metal-Oxide-Silicon (EPIC-MOS), European Photon Imaging Camera-PN (EPIC-PN) and Reflection Grating Spectrometer. EPIC-MOS (MOS1, MOS2) and EPIC-PN provide relatively good spectral resolutions ($E/dE \sim 50$) at 6.5 keV, which are suitable to measure the $I_{7.0}/I_{6.7}$.

We start by searching the XMM-Newton archive for observations of CVs in Ritter & Kolb (2003)'s catalog (Final edition 7.24) and of some IPs recently discovered (de Martino et al. 2020) within 5′ off-axis angles, and obtain 419 observations on 247 CVs. As the next step, CVs whose $I_{7.0}/I_{6.7}$ could not be well constrained (see the next paragraph for details) are excluded from the sample (e.g., AB Dra, TY PsA; some other sources without enough net counts are also excluded due to low Fe abundance, e.g., V2731 Oph), which results in a sample of 113 observations on 83 CVs including 20 DNe, 36 IPs, 18 Polars and nine nova-likes. Then we remove CVs in non-quiescent states[1] from the sample, and exclude polars and nova-likes (which may have different $I_{7.0}/I_{6.7}$–$M_{\rm WD}$ relations). Furthermore, EX Hya and GK Per have extremely low magnetospheric radii (Suleimanov et al. 2016, 2019), which cause lower shock temperatures and lead to lower derived WD masses, so they are removed from the sample. Finally, we get a sample of 48 CVs from XMM-Newton, as listed in Table 1. We also include a sample of 26 quiescent IPs and DNe observed by Suzaku from Xu et al. (2019b) and Yu et al. (2018), where sources with weak FeXXV-Heα and FeXXVI-Lyα lines are removed. The Suzaku CV sample is listed in Table 2.

All observations on sampled CVs are then reprocessed with Science Analysis System (SAS, v16.1.0) software with the latest calibration files. Good time intervals are chosen by removing flares at the energy of >10 keV, which are decided by critical values which vary for different observations. The typical critical values are 0.35 cts s^{-1} and 0.8 cts s^{-1} for MOS and PN chips, respectively. For most observations, source events are extracted from a 40″ circular region centered at the source, and backgrounds from a circular, source-free region of the same size on the same chip, respectively. Specifically, the source and background region radii are reduced to 20″–30″ if the MOS CCDs were operated in the Small Window mode or there are contaminated sources. If potential pile-up occurs[2] source counts will be extracted from an annulus with typical inner radius of 5″. The spectra are then regrouped to ensure a signal-to-noise ratio of three per bin at least.

We then measure the $I_{7.0}/I_{6.7}$ of individual CVs by jointly fitting the 5–8 keV background-subtracted spectra from MOS1, MOS2 and PN detectors. The fitting is performed with the model phabs(apec+threeGaussian) in Xspec 12.10.1, where the abundance of apec is set to 0. In this model, the apec component represents the X-ray continuum of the CVs,[3] and the threeGaussian model was built specifically to measure the $I_{7.0}/I_{6.7}$ (Xu et al. 2016). We fix all line width values to 1.0×10^{-5} keV following Xu et al. (2016), since the spectral resolution is not enough to constrain them.

The fitting results are shown in Table 3, where the $I_{7.0}/I_{6.7}$ from Suzaku observations by Xu et al. (2016) and Xu et al. (2019b) are listed for comparison. Two examples of the XMM-Newton fitting are plotted in Figure 1.

From Tables 1 and 2, 16 CVs (including 11 IPs and five DNe) have both XMM-Newton and Suzaku observations. By merging the two samples, we have a final sample of 58 individual CVs, including 36 IPs and 22 DNe.

3. WD Mass Derivation

3.1. Updating the T_{max}–M_{WD} Relation for DNe

The previous semi-empirical $T_{\rm max}$–$M_{\rm WD}$ relation (i.e., Equation (2)) for DNe was obtained based on $T_{\rm max}$ measurements with Suzaku observations. Those $T_{\rm max}$ values could be biased due to the limited counting statistics above 10 keV caused by the high background level of the Suzaku HXD detector. With the recently available NuSTAR observations, it is now possible to update the $T_{\rm max}$, and thus the $T_{\rm max}$–$M_{\rm WD}$ relation for DNe. Additionally, in previous works (e.g., Yu et al. 2018; Xu et al. 2019b), $T_{\rm max}$ were measured with the mkcflow model with the mekal description with the old atomic database (parameter "switch" set to 1), thus the measured $T_{\rm max}$ may be different from the ones when using the apec description with AtomDB (parameter "switch" set to 2, where the latest AtomDB is incorporated). We then fit the spectra of Suzaku and NuSTAR observed CVs again by switching the emission description to apec, and summarize the measured $T_{\rm max}$ in

[1] The states in most observations are determined using the American Association of Variable Star Observers (AAVSO) International Database. If no data was found in AAVSO, the states are inferred from the light curves from multiple observations of the same source.

[2] Procedure of testing pile-up is from https://www.cosmos.esa.int/web/xmm-newton/sas-thread-epatplot.

[3] We use apec instead of mekal here because the latter has been used in Xu et al. (2016). We also tried to use mkcflow or bremsstrahlung for continuum and find the differences of the resulting $I_{7.0}/I_{6.7}$ are within 5%.

Table 1
Observation Log and Dynamically Measured WD Masses of CVs Observed by XMM-Newton

Source	Coordinate (J2000)		Obs ID	Type	Pile-up	M_{WD}
	R.A.	Decl.			(Y/N)	($M_{\odot}$)
WW Cet	00:11:25	−11:28:43	111970901	DN	N	0.83 ± 0.16[1]
HT Cas	01:10:13	+60:04:36	111310101	DN	N	0.61 ± 0.04[2]
VW Hyi	04:09:11	−71:17:41	111970301	DN	N	0.67 ± 0.22[3]
SS Aur	06:13:22	+47:44:26	502640201	DN	N	1.08 ± 0.4[4]
U Gem	07:55:05	+22:00:06	110070401	DN	N	1.2 ± 0.05[5]
Z Cha	08:07:28	−76:32:01	205770101	DN	N	0.84 ± 0.09[6]
YZ Cnc	08:10:57	+28:08:34	152530101	DN	N	0.82 ± 0.08[7]
SU UMa	08:12:28	+62:36:23	111970801	DN	Y	⋯
OY Car	10:06:22	−70:14:05	99020301	DN	N	0.685 ± 0.011[8]
QZ Vir	11:38:27	+03:22:08	111970701	DN	N	0.375 ± 0.025[9]
V1129 Cen	12:39:08	−45:33:44	500440101	DN	N	⋯
V893 Sco	16:15:15	−28:37:31	553720101	DN	N	0.89 ± 0.15[10]
V426 Oph	18:07:52	+05:51:49	306290101	DN	Y	0.9 ± 0.19[11]
SS Cyg	21:42:43	+43:35:10	791000201	DN	Y	1.1 ± 0.2[12]
RU Peg	22:14:03	+12:42:11	551920101	DN	N	1.06 ± 0.04[13]
V405 Peg	23:09:49	+21:35:18	604060101	DN	N	⋯
V1033 Cas	00:22:58	+61:41:08	501230201	IP	N	⋯
V709 Cas	00:28:49	+59:17:22	743120401	IP	N	⋯
V515 And	00:55:20	+46:12:57	501230301	IP	N	⋯
XY Ari	02:56:08	+19:26:34	501370101	IP	N	1.04 ± 0.13[14]
2MASS J04570832+4527499	04:57:08	+45:27:50	721790201	IP	N	⋯
RX J0525.3+2413	05:25:23	+24:13:34	721790301	IP	N	⋯
MU Cam	06:25:16	+73:34:40	207160101	IP	N	⋯
V647 Aur	06:36:33	+35:35:43	551430601	IP	N	⋯
PQ Gem	07:51:17	+14:44:25	109510301	IP	N	⋯
HT Cam	07:57:01	+63:06:01	144840101	IP	N	⋯
DW Cnc	07:58:53	+16:16:45	673140101	IP	N	⋯
EI UMa	08:38:22	+48:38:02	111971701	IP	N	⋯
Swift J0927.7-6945	09:27:53	−69:44:42	761120901	IP	N	⋯
V1025 Cen	12:38:17	−38:42:46	673140501	IP	N	⋯
VVV J140845.99-610754.1	14:08:46	−61:07:56	761940301	IP	N	⋯
2MASS J15092601-6649232	15:09:26	−66:49:23	551430301	IP	N	⋯
NY Lup	15:48:15	−45:28:40	105460301	IP	N	⋯
2MASS J16495517-3307088	16:49:56	−33:07:02	601270401	IP	N	⋯
Swift J1701.3-4304	17:01:28	−43:06:12	761120701	IP	N	⋯
V2400 Oph	17:12:36	−24:14:45	105460101	IP	Y	⋯
CXOU J171935.8-410053	17:19:36	−41:00:54	601270201	IP	Y	⋯
2MASS J18043892-1456474	18:04:39	−14:56:47	405390301	IP	N	⋯
IGR J18173-2509	18:17:22	−25:08:43	601270301	IP	N	⋯
IGR J18308-1232	18:30:50	−12:32:19	601270501	IP	N	⋯
AX J1832.3-0840	18:32:19	−08:40:30	511010801	IP	N	⋯
XMMU J185330.7-012815	18:53:31	−01:28:16	201500301	IP	N	⋯
V1223 Sgr	18:55:02	−31:09:49	145050101	IP	N	⋯
1RXS J211336.1+542226	21:13:35	+54:22:33	761120801	IP	N	⋯
V2069 Cyg	21:23:45	+42:18:02	601270101	IP	N	⋯
RX J2133.7+5107	21:33:44	+51:07:25	302100101	IP	N	⋯
FO Aqr	22:17:55	−08:21:05	9650201	IP	N	⋯
AO Psc	22:55:18	−03:10:40	9650101	IP	Y	⋯

M_{WD} references: 1. Fertig et al. (2011); 2. Horne et al. (1991); 3. Hamilton et al. (2011); 4. Sion et al. (2008); 5. Ritter & Kolb (2003); 6. Wade & Horne (1988); 7. Shafter & Hessman (1988); 8. Wood et al. (1989); 9. Shafter & Szkody (1984); 10. Mason et al. (2001), where a 0.15 $M_{\odot}$ uncertainty is assumed; 11. Hessman (1988); 12. Friend et al. (1990); 13. Dunford et al. (2012); 14. Hellier (1997), the WD mass was not dynamically measured, but considered as a reliable measurement in most previous works (e.g., Yuasa et al. 2010; Suleimanov et al. 2019).

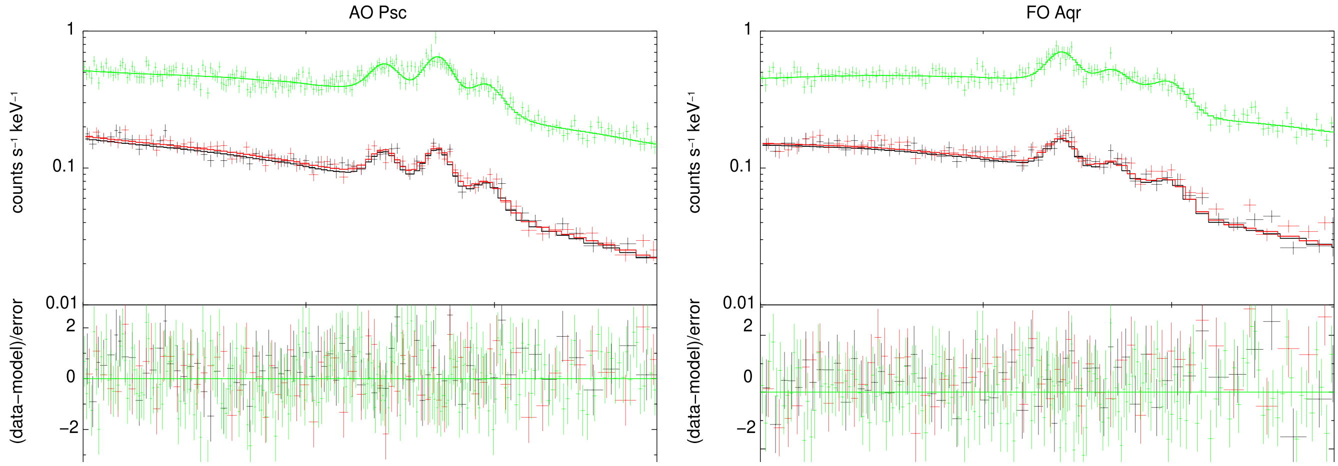

Figure 1. The best-fit XMM-Newton 5–8 keV spectra of AO Psc and FO Aqr. The black, red and green data points represent spectra from MOS-1, MOS-2 and PN, respectively. Spectra are rebinned for plotting only.

Table 2
Observation Log and Dynamically Measured WD Masses of CVs Observed by Suzaku

Source	Coordinate (J2000)		Obs ID	Type	M_{WD}
	R.A.	Decl.			($M_{\odot}$)
VW Hyi	04:09:11	−71:17:41	406009030	DN	0.67 ± 0.22[1]
V1159 Ori	05:28:60	−03:33:53	408029010	DN	⋯
FS Aur	05:47:48	+28:35:11	408041010	DN	⋯
SS Aur	06:13:22	+47:44:26	402045010	DN	1.08 ± 0.4[2]
U Gem	07:55:05	+22:00:06	407034010	DN	1.2 ± 0.05[3]
BZ UMa	08:53:44	+57:48:41	402046010	DN	0.65 ± 0.15[4]
CH UMa	10:07:01	+67:32:47	407043010	DN	⋯
BV Cen	13:31:20	−54:58:34	407047010	DN	1.24 ± 0.22[5]
EK TrA	15:14:01	−65:05:35	407044010	DN	0.46 ± 0.1[6]
V893 Sco	16:15:15	−28:37:31	401041010	DN	0.89 ± 0.15[7]
SS Cyg	21:42:43	+43:35:10	400006010	DN	1.1 ± 0.2[8]
V709 Cas	00:28:49	+59:17:22	403025010	IP	⋯
XY Ari	02:56:08	+19:26:34	500015010	IP	1.04 ± 0.13[9]
TV Col	05:29:25	−32:49:05	403023010	IP	0.75 ± 0.15[10]
TX Col	05:43:20	−41:01:55	404031010	IP	⋯
MU Cam	06:25:16	+73:34:40	403004010	IP	⋯
BG CMi	07:31:29	+09:56:23	404029010	IP	0.8 ± 0.2[11]
PQ Gem	07:51:17	+14:44:25	404030010	IP	⋯
YY Dra	11:43:38	+71:41:20	403022010	IP	0.83 ± 0.1[12]
NY Lup	15:48:15	−45:28:40	401037010	IP	⋯
V2400 Oph	17:12:36	−24:14:45	403021010	IP	⋯
CXOU J171935.8-410053	17:19:36	−41:00:54	403028010	IP	⋯
V1223 Sgr	18:55:02	−31:09:49	408019020	IP	⋯
RX J2133.7+5107	21:33:44	+51:07:25	401038010	IP	⋯
FO Aqr	22:17:55	−08:21:05	404032010	IP	⋯
AO Psc	22:55:18	−03:10:40	404033010	IP	⋯

M_{WD} references: 1. Hamilton et al. (2011); 2. Sion et al. (2008); 3. Ritter & Kolb (2003); 4. Jurcevic et al. (1994); 5. Watson et al. (2007); 6. Gänsicke et al. (1997); 7. Mason et al. (2001), where a 0.15 $M_{\odot}$ uncertainty is assumed; 8. Friend et al. (1990); 9. Hellier (1997), the WD mass was not dynamically measured, but considered as a reliable measurement in most previous works (e.g., Yuasa et al. 2010; Suleimanov et al. 2019); 10. Hellier (1993); 11. Penning (1985); 12. Haswell et al. (1997).

Table 4, where $T_{\rm max}$ from previous works are also listed for comparison. We further refit the $T_{\rm max}$–$M_{\rm WD}$ relation in Equation (2) with the new $T_{\rm max}$ using the orthogonal distance regression (ODR) method, where he mean molecular weight μ is fixed at 0.6 (e.g., Byckling et al. 2010) and $R_{\rm WD}$ is derived from WD's $M_{\rm WD}$–$R_{\rm WD}$ relation (Nauenberg 1972). The fitting yields an $\alpha = 0.69 \pm 0.06$ (shown in Figure 2) with $\chi^2_\nu = 0.66$, which is consistent with previous one ($\alpha = 0.646 \pm 0.069$), and will be used in the rest of the paper.

3.2. Updating the $I_{7.0}/I_{6.7}$–T_{max} and the $I_{7.0}/I_{6.7}$–M_{WD} Relations

Similar to $T_{\rm max}$, the previous $I_{7.0}/I_{6.7}$–$T_{\rm max}$ and $I_{7.0}/I_{6.7}$–$M_{\rm WD}$ relations were also based on $I_{7.0}/I_{6.7}$ values measured with the mkcflow model with the mekal description. We thus verify these relations with mkcflow with the apec description as follows.

First, we obtain the $I_{7.0}/I_{6.7}$–$T_{\rm max}$ relations derived from the mkcflow model with apec description following Xu et al. (2019a), and compare them with the observed values in Figure 3. The data points are from Table 4. Obviously, the observed $I_{7.0}/I_{6.7}$ and $T_{\rm max}$ still follow the updated $I_{7.0}/I_{6.7}$–$T_{\rm max}$ relation.

Second, we examine the $I_{7.0}/I_{6.7}$–$M_{\rm WD}$ relations. We plot the $I_{7.0}/I_{6.7}$ and the dynamically measured $M_{\rm WD}$ of sampled CVs in Figure 4. We also plot the $I_{7.0}/I_{6.7}$–$M_{\rm WD}$ relations derived by combining Equation (1) or Equation (2) and the mkcflow with mekal and apec descriptions in Figure 4 for comparison. From the figure, the $I_{7.0}/I_{6.7}$–$M_{\rm WD}$ curves of both the mekal and apec description can well describe the sampled DNe. On the other hand, the IPs are more consistent with the apec description. We suspect that it is because the AtomDB used by apec description works better for the high $I_{7.0}/I_{6.7}$ case, where most IPs are located. It is also worth noticing that a $I_{7.0}/I_{6.7}$ may refer to different $M_{\rm WD}$ (and $T_{\rm max}$) values for different metallicity Z.

3.3. The New Spectral Model to Measure WD Masses

We introduce a new model to replace the threeGaussian model, so that the fitting of the 5–8 keV spectra could measure $T_{\rm max}$ (from the $I_{7.0}/I_{6.7}$–$T_{\rm max}$ relations shown in Figure 3) and output $M_{\rm WD}$ (from the $T_{\rm max}$–$M_{\rm WD}$ relations shown in Equations (1) and (2)) directly. The new model are divided to two sub-models: ipmass_line and dnmass_line, according to the different $T_{\rm max}$–$M_{\rm WD}$ relations (Equations (1) and (2)) for IPs and DNe, respectively. In Equations (1) and (2), the mean molecular weight μ is fixed at 0.6 (e.g., Byckling et al. 2010) and $R_{\rm WD}$ is derived from WD's $M_{\rm WD}$–$R_{\rm WD}$ relation (Nauenberg 1972). Thus the model only contains two free parameters: the WD mass ($M_{\rm WD}$) and the abundance (Z). The latter has to be

Table 3
$I_{7.0}/I_{6.7}$ of XMM-Newton Observed CVs

Source	Type	$I_{7.0}/I_{6.7}$ [a]	χ^2_ν(d.o.f.)	$I_{7.0}/I_{6.7}$ [b]
WW Cet	DN	$0.23^{+0.16}_{-0.15}$	0.97(249)	…
HT Cas	DN	$0.28^{+0.10}_{-0.11}$	0.98(234)	…
VW Hyi	DN	$0.23^{+0.11}_{-0.07}$	1.02(132)	0.21 ± 0.07
SS Aur	DN	$0.58^{+0.25}_{-0.24}$	1.08(112)	0.56 ± 0.2
U Gem	DN	$0.63^{+0.13}_{-0.07}$	0.84(379)	0.68 ± 0.08
Z Cha	DN	$0.22^{+0.05}_{-0.06}$	1.01(656)	…
YZ Cnc	DN	$0.38^{+0.06}_{-0.07}$	1.00(317)	…
SU UMa	DN	$0.58^{+0.27}_{-0.24}$	0.82(140)	…
OY Car	DN	$0.24^{+0.05}_{-0.05}$	0.96(465)	…
QZ Vir	DN	$0.13^{+0.10}_{-0.11}$	1.07(183)	…
V1129 Cen	DN	$0.30^{+0.15}_{-0.18}$	1.02(135)	…
V893 Sco	DN	$0.27^{+0.04}_{-0.04}$	1.10(854)	0.37 ± 0.07
V426 Oph	DN	$0.58^{+0.05}_{-0.05}$	1.01(890)	…
SS Cyg	DN	$0.64^{+0.14}_{-0.12}$	1.03(784)	0.73 ± 0.07
RU Peg	DN	$0.70^{+0.09}_{-0.10}$	0.99(879)	…
V405 Peg	DN	$0.19^{+0.16}_{-0.14}$	1.04(77)	…
V1033 Cas	IP	$0.65^{+0.41}_{-0.28}$	0.93(421)	…
V709 Cas	IP	$1.23^{+0.70}_{-0.31}$	1.07(884)	0.97 ± 0.20
V515 And	IP	$0.82^{+0.17}_{-0.16}$	0.92(745)	…
XY Ari	IP	$1.09^{+0.68}_{-0.41}$	0.91(407)	0.94 ± 0.2
2MASS J04570832+4527499	IP	$1.32^{+1.24}_{-0.59}$	0.92(656)	…
RX J0525.3+2413	IP	$0.93^{+1.34}_{-0.57}$	0.97(393)	…
MU Cam	IP	$0.67^{+0.85}_{-0.50}$	0.71(98)	1.03 ± 0.18
V647 Aur	IP	$1.03^{+1.92}_{-0.41}$	0.84(245)	…
PQ Gem	IP	$0.67^{+0.31}_{-0.26}$	0.86(846)	0.77 ± 0.26
HT Cam	IP	$0.88^{+0.54}_{-0.40}$	0.95(139)	…
DW Cnc	IP	$0.59^{+0.28}_{-0.22}$	0.87(233)	…
EI UMa	IP	$0.58^{+0.24}_{-0.11}$	0.92(522)	…
Swift J0927.7-6945	IP	$0.98^{+0.40}_{-0.32}$	1.16(289)	…
V1025 Cen	IP	$0.44^{+0.19}_{-0.18}$	1.03(271)	…
VVV J140845.99-610754.1	IP	$0.81^{+0.43}_{-0.48}$	1.13(104)	…
2MASS J15092601-6649232	IP	$0.70^{+0.30}_{-0.25}$	1.01(797)	…
NY Lup	IP	$0.88^{+0.19}_{-0.12}$	0.98(869)	1.03 ± 0.16
2MASS J16495517-3307088	IP	$1.12^{+0.32}_{-0.25}$	0.85(624)	…
Swift J1701.3-4304	IP	$0.87^{+0.43}_{-0.28}$	0.90(353)	…
V2400 Oph	IP	$0.98^{+0.65}_{-0.39}$	0.95(507)	0.73 ± 0.05
CXOU J171935.8-410053	IP	$0.95^{+0.29}_{-0.23}$	1.00(912)	0.87 ± 0.20
2MASS J18043892-1456474	IP	$0.98^{+0.38}_{-0.28}$	0.95(274)	…
IGR J18173-2509	IP	$0.26^{+0.26}_{-0.24}$	0.98(805)	…
IGR J18308-1232	IP	$0.61^{+0.24}_{-0.20}$	0.97(496)	…
AX J1832.3-0840	IP	$0.73^{+0.21}_{-0.19}$	0.92(578)	…
XMMU J185330.7-012815	IP	$0.59^{+0.24}_{-0.20}$	0.89(183)	…
V1223 Sgr	IP	$0.76^{+0.14}_{-0.12}$	1.09(979)	0.8 ± 0.08
1RXS J211336.1+542226	IP	$0.74^{+0.17}_{-0.17}$	0.93(352)	…
V2069 Cyg	IP	$0.78^{+0.74}_{-0.43}$	0.86(438)	…
RX J2133.7+5107	IP	$0.89^{+0.65}_{-0.41}$	0.94(680)	0.88 ± 0.11
FO Aqr	IP	$0.64^{+0.26}_{-0.22}$	0.95(958)	0.58 ± 0.12
AO Psc	IP	$0.40^{+0.06}_{-0.05}$	0.97(979)	0.48 ± 0.08[a]

Notes.
a The flux ratios of the Fe XXVI–Lyα to Fe XXV–Heα lines measured with XMM-Newton data and Suzaku data in this work, respectively.
[b] We have repeated the flux ratio measurements for all the Suzaku observed CVs using the latest calibration files, and find most of the new measurements are within 5%–10% of the previous ones by Xu et al. (2016). The only exception is AO Psc, where the new value (0.48 ± 0.08) is about 14% off the previous measurements (0.56 ± 0.06), which is most likely due to the new calibration files used in this work. We then adopt the 0.48 ± 0.08 as the flux ratio measured by Suzaku here.

Table 4
Maximum Emission Temperature (T_{max}) and $I_{7.0}/I_{6.7}$ Measured with NuSTAR and Suzaku data, and Dynamically Determined mass (M_{WD}) of CVs

Source	NuSTAR ObsID	Suzaku ObsID	T_{max}[a] (keV)	χ^2_ν(d.o.f.)	T_{max}[b] (keV)	M_{WD}[c] ($M_\odot$)	$I_{7.0}/I_{6.7}$[d]
			IPs				
BG CMi	30460018002	⋯	$36.6^{+5.8}_{-4.6}$	0.89(967)	32.5 ± 6.0	0.8 ± 0.2[f]	0.71 ± 0.18
EX Hya	30201016002	⋯	$14.3^{+0.7}_{-0.8}$	1.03(875)	14.5 ± 0.3	0.790 ± 0.026[g]	0.39 ± 0.02
TV Col	30001020002	⋯	$31.8^{+2.8}_{-2.1}$	1.01(1217)	30.1 ± 2.1	0.75 ± 0.15[h]	0.67 ± 0.08
XY Ari	30460006002	⋯	$86.2_{-20.5}$	0.94(233)	57.5 ± 7.9	1.04 ± 0.13[i]	0.94 ± 0.20
AO Psc	30460008002	⋯	$17.6^{+1.3}_{-1.0}$	1.12(992)	17.9 ± 1.2	⋯	0.48 ± 0.08[e]
FO Aqr	30460002002	⋯	$23.5^{+2.1}_{-2.0}$	1.14(990)	22.3 ± 1.5	⋯	0.58 ± 0.12
CXOU J171935.8-410053	30460005002	⋯	$38.9^{+7.0}_{-5.2}$	1.03(971)	37.8 ± 4.8	⋯	0.87 ± 0.20
RX J2133.7+5107	30460001002	⋯	$50.5^{+13.1}_{-8.2}$	1.05(995)	47.3 ± 7.5	⋯	0.88 ± 0.11
NY Lup	30001146002	⋯	$66.0^{+10.4}_{-10.9}$	0.95(1126)	53.2 ± 5.1	⋯	1.03 ± 0.16
V709 Cas	30001145002	⋯	$47.1^{+9.6}_{-7.0}$	0.96(1009)	43.5 ± 6.8	⋯	0.97 ± 0.20
V1223 Sgr	30001144002	⋯	$33.6^{+2.2}_{-1.6}$	1.06(1257)	32.4 ± 2.5	⋯	0.80 ± 0.08
V2400 Oph	30460003002	⋯	$23.8^{+2.4}_{-2.1}$	1.03(1032)	30.9 ± 2.0	⋯	0.73 ± 0.05
			DNe				
V893 Sco	⋯	401041010	$16.0^{+1.1}_{-1.2}$	0.91(2774)	15.7 ± 1.1	0.89 ± 0.15[j]	0.37 ± 0.07
SS Aur	⋯	402045010	$28.5^{+2.2}_{-4.2}$	0.91(921)	26.3 ± 2.9	1.08 ± 0.40[k]	0.56 ± 0.20
BZ UMa	30201019002	⋯	$10.7^{+3.3}_{-2.5}$	1.00(293)	13.6 ± 0.4	0.65 ± 0.15[l]	0.40 ± 0.16
VW Hyi	⋯	406009030	$9.9^{+0.4}_{-0.4}$	1.02(1535)	9.7 ± 0.5	0.67 ± 0.22[m]	0.21 ± 0.07
UGem	⋯	407034010	$28.5^{+0.8}_{-1.8}$	1.05(3391)	26.9 ± 0.6	1.20 ± 0.05[n]	0.68 ± 0.08
EK TrA	⋯	407044010	$8.5^{+0.4}_{-0.4}$	1.06(2438)	10.4 ± 0.5	0.46 ± 0.10[o]	0.16 ± 0.08
BV Cen	⋯	407047010	$27.1^{+3.8}_{-3.0}$	1.05(2878)	25.1 ± 2.2	1.24 ± 0.22[p]	0.55 ± 0.10[e]
SS Cyg	80202036002	⋯	$24.3^{+1.5}_{-0.7}$	0.95(879)	26.9 ± 1.4	1.1 ± 0.2[q]	0.73 ± 0.07
SW UMa	⋯	402044010	$8.2^{+0.7}_{-1.1}$	0.95(661)	7.8 ± 0.6	0.71 ± 0.22[r]	⋯
CH UMa	⋯	407043010	$14.4^{+0.9}_{-0.9}$	0.99(1700)	14.3 ± 0.8	⋯	0.36 ± 0.11
V1159 Ori	⋯	408029010	$9.3^{+0.4}_{-0.4}$	1.03(1861)	9.3 ± 0.6	⋯	0.16 ± 0.14
FS Aur	⋯	408041010	$22.0^{+2.2}_{-1.9}$	0.96(1706)	21.1 ± 1.8	⋯	0.40 ± 0.21

Notes.
[a] T_{max} from this work.
[b] T_{max} from Xu et al. (2019b) and Yu et al. (2018).
[c] Dynamically determined M_{WD}.
[d] $I_{7.0}/I_{6.7}$ from Xu et al. (2019b) and Xu et al. (2016).
[e] $I_{7.0}/I_{6.7}$ is re-measured in this work.
[f] Penning (1985).
[g] Beuermann & Reinsch (2008).
[h] Hellier (1993).
[i] Hellier (1997).
[j] Mason et al. (2001).
[k] Sion et al. (2008).
[l] Jurcevic et al. (1994).
[m] Hamilton et al. (2011).
[n] Ritter & Kolb (2003).
[o] Gänsicke et al. (1997).
[p] Watson et al. (2007).
[q] Friend et al. (1990).
[r] Ritter & Kolb (2003).

constrained first because the $I_{7.0}/I_{6.7}$–T_{max} relations are abundance dependent, as shown in Figure 3.

To use this model, we first constrain the uncertainty ranges of Z by fitting the 5–8 keV spectra with the cooling flow model: phabs(mkcflow+Gauss) (the Gaussian components describe the Fe I–Kα lines) with the apec description. Then we only allow Z of the new models to vary within the uncertainty ranges derived from previous step (Typical abundance ∼0.1 and

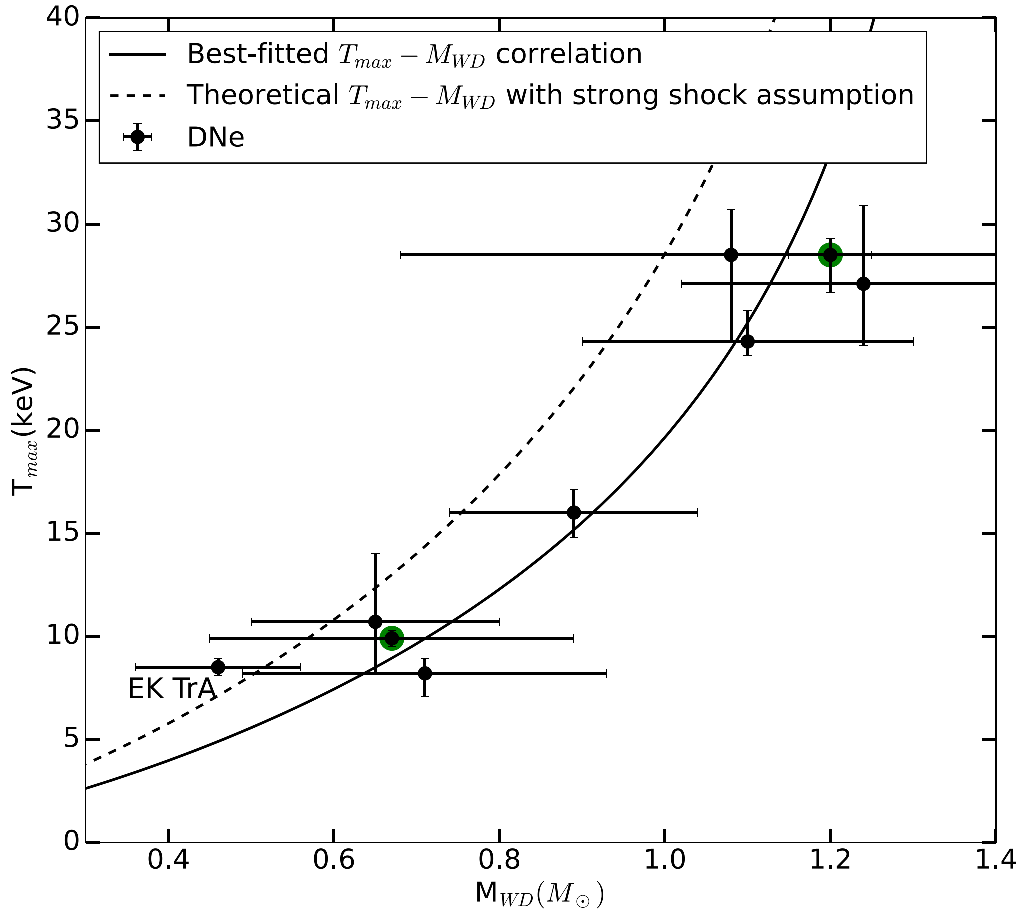

Figure 2. The semi-empirical $T_{\max}$ –$M_{\rm WD}$ relation (Equation (2)) for DNe. The solid curve shows the updated $T_{\max}$ –$M_{\rm WD}$ relation with $\alpha = 0.69$ and the dashed curve shows the case with the strong shock assumption ($\alpha = 1$). Points surrounded by green represent Zorotovic et al. (2011)'s fiducial sub-sample of "robust dynamical mass measurements".

$\sim$0.3 $Z_\odot$ for luminous and dim sources, respectively), and refit the 5–8 keV spectra with phabs(apec+ipmass_line+Gauss) or phabs(apec+dnmass_line+Gauss) for IPs and DNe, respectively. During the fitting the abundance of apec is fixed to 0, just like the case for the threeGaussian model. The output $M_{\rm WD}$ values are summarized in Tables 5 and 6, where the upper limit of all derived WD masses is assumed to 1.44 $M_\odot$.

3.4. WD Mass Distribution in CVs

From Table 6, the $M_{\rm WD}$ derived from XMM-Newton and Suzaku data for same CVs are consistent with each other. We then build a sample of 58 individual CVs with $M_{\rm WD}$ measurements, including 22 DNe and 36 IPs from Tables 5 and 6. We adopt Suzaku measured $M_{\rm WD}$ if there are measurements from both XMM-Newton and Suzaku, because the latter usually provides higher quality spectra and therefore lower uncertainties.

The distribution of WD masses in sampled IPs and DNe are plotted in Figure 5. From the figure, WD masses in both IPs and DNe are distributed in a wide range, from $\sim$0.4–0.5 $M_\odot$ to $\sim$1.2 $M_\odot$ and peaking at $\sim$0.8 $M_\odot$. There might be hints of a second peak at $\sim$1.1–1.2 $M_\odot$ for DNe, but the statistics is too low to draw any firm conclusion. The mean WD masses in IPs and DNe can be calculated to be $\langle M_{\rm WD,IP}\rangle = 0.81 \pm 0.21\, M_\odot$ and $\langle M_{\rm WD,DN}\rangle = 0.81 \pm 0.21\, M_\odot$, respectively. We also examine the distribution of WD masses in IPs and DNe with a Kolmogorov–Smirnov test, and the two-sided p-value is $\sim$0.92. In other words, we do not find systematical differences between the distribution of WD masses in IPs and DNe.

4. Discussion

4.1. Comparison with Previous Works

First, we check the reliability of our measured $I_{7.0}/I_{6.7}$. At first, iron absorption edge in CVs may influence the measurement of $I_{7.0}/I_{6.7}$. We add an iron absorption edge component, where the absorption depth is set to 0.1 at 7.11 keV (Nobukawa et al. 2016, mean absorption depth is 0.02 ± 0.01

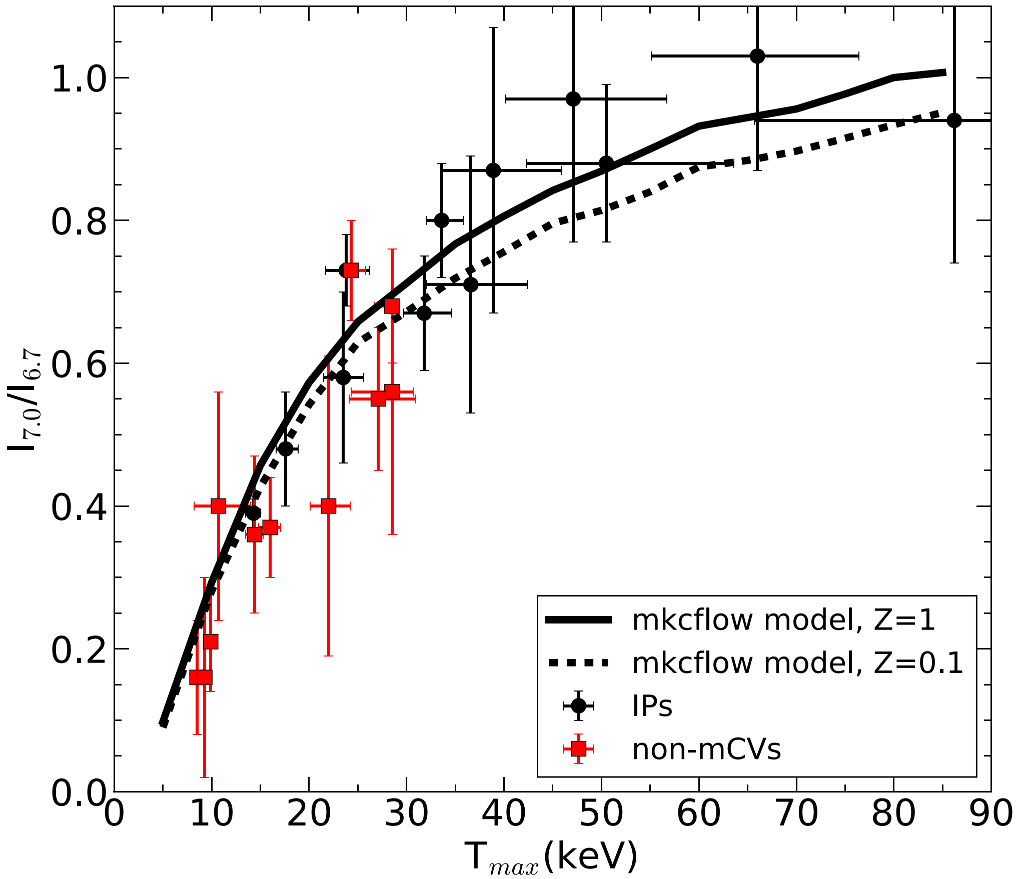

Figure 3. $I_{7.0}/I_{6.7}$ versus $T_{\max}$ for CVs. The solid and dashed curves are relations predicted by the mkcflow model with apec description and with $Z = 1Z_{\odot}$ and $Z = 0.1Z_{\odot}$, respectively. Black and red points represent IPs and DNe, respectively.

and 0.08 ± 0.04 for IPs and non-mCVs, respectively), and perform spectral fitting again. The results show that the new $I_{7.0}/I_{6.7}$ are consistent with previous measurements.[4] We further compare the $I_{7.0}/I_{6.7}$ values measured in this work with those in previous works like Ezuka & Ishida (1999) and Rana et al. (2006) using ASCA and Chandra HETG observations, and they are again consistent with each other. Moreover, our $I_{7.0}/I_{6.7}$ from XMM-Newton observations are consistent with those based on Suzaku observations (Xu et al. 2016, 2019b), as shown in Table 3 and Figure 6. Considering the fact that these measurements are made with different instruments (XMM-Newton, Suzaku, Chandra–HETG and ASCA) in a time range spanning ∼20 yr, the consistency indicates the robustness of $I_{7.0}/I_{6.7}$, which is one of the essential quality to be used as a diagnostic for $M_{\rm WD}$.

Second, we check the possible bias brought by the uncertainties in previous WD mass measurements. Following Zorotovic et al. (2011), we considered WD mass measurements on VW Hyi, U Gem, HT Cas, OY Car, Z Cha as "robust" ones, and manually add 20% systematic errors for other sources. We then perform best-fit for Equation (2), and the result shows $\alpha = 0.67 \pm 0.06$, which is consistent with the previous value ($\alpha = 0.69 \pm 0.06$), and there is no significant influence on $I_{7.0}/I_{6.7}$–$T_{\max}$–$M_{\rm WD}$ relations.

Third, we compare our derived $M_{\rm WD}$ with those from Suleimanov et al. (2019), who derived $M_{\rm WD}$ of IPs with the continuum fitting method based on NuSTAR and Swift observations.[5] There are 25 CVs included in both their and our samples. The results of 21 CVs are consistent with ours except for the other four CVs: $M_{\rm WD} = 0.67 \pm 0.08\,M_{\odot}$ for MU Cam, $M_{\rm WD} = 0.72 \pm 0.02\,M_{\odot}$ for V1223 Sgr, $M_{\rm WD} = 1.05 \pm 0.04\,M_{\odot}$ for NY Lup and $M_{\rm WD} = 0.72 \pm 0.06\,M_{\odot}$ for CXOU J171935.8-410053. Our results are $1.09^{+0.31}_{-0.29}\,M_{\odot}$, $0.92^{+0.15}_{-0.12}\,M_{\odot}$, $0.82^{+0.14}_{-0.09}\,M_{\odot}$ and $1.08^{+0.32}_{-0.24}\,M_{\odot}$ in MU Cam, V1223 Sgr, NY Lup and CXOU J171935.8-410053, respectively. The

[4] No absorption edge component were included in previous measurements, which is equivalent to zero absorption depth here.

[5] We utilize NuSTAR to derive WD masses of IPs with cooling flow model and post-shock region (PSR) model developed by Suleimanov et al. (2016), and the typical WD mass difference is within 5%.

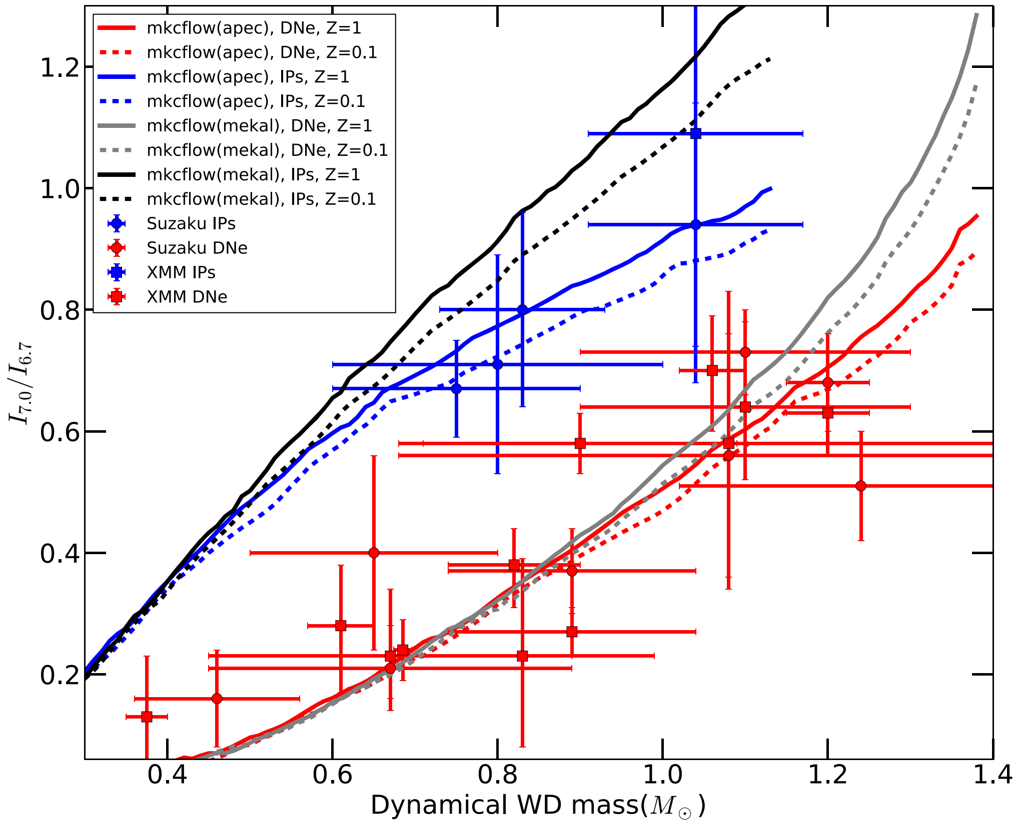

Figure 4. $I_{7.0}/I_{6.7}$ versus dynamically determined $M_{\rm WD}$ for sampled CVs. The blue (red) solid curves are the predicted relations for IPs (DNe) from Equations (1) and (2) by the mkcflow model.

differences may be explained as follows: First, we assume the accreted material falls from infinity, while in reality they could fall from a certain distance, e.g., the inner radius of the truncated accretion disk, leading to underestimation of $M_{\rm WD}$. Second, the Compton hump (∼10–30keV) caused by the reflection (Mukai et al. 2015) could soften the hard X-ray continuum, which would lead to a lower temperature than ours, thus a lower WD mass. Third, a different local mass accretion rate, fixed at 1 g s^{-1} cm^{-2} in Suleimanov et al. (2019), could affect the hard X-ray continuum (Suleimanov et al. 2016), leading to a deviation of $M_{\rm WD}$. Similar reasons could also be responsible for the difference between our results and those of Yuasa et al. (2010). Additionally, we notice our derived WD masses have larger errors than those in Suleimanov et al. (2019). The uncertainties of the derived WD masses are mainly related to the uncertainties of the measured flux ratios, which is determined by the counting statistics of the spectra in the Fe line energy range. On the other hand, as discussed in Section 1, the method in this work make use of the large archival observations on CV by XMM-Newton and Suzaku which allows a larger sample size compared to previous works using hard X-ray (up to 30–50 keV) observations.

Fourthly, we compare the $M_{\rm WD}$ derived from the new models (ipmass_line or dnmass_line) with the dynamical results in Figure 7 and in Tables 5 and 6. The comparison shows that the derived masses of all the 20 CVs are consistent with the dynamical values. Moreover, we make a quantitative examination on the goodness of the new model derived $M_{\rm WD}$. Following Xu et al. (2019b)'s method, we assume a linear relation in the form of $M_{\rm WD,derived} = A \times M_{\rm WD,dynamical} + B$ (For a good relation, we expect $A \sim 1$ and $B \sim 0$.) and perform fitting with the ODR method. The best-fitted results are plotted in Figure 7 to be compared with observed values. For the 11 Suzaku sampled CVs mentioned in Xu et al. (2019b), the best-fit yields $A = 0.86 \pm 0.16$, $B = 0.08 \pm 0.15$ and $r^2 = 0.95$, which are consistent with the previous values ($A = 0.97 \pm 0.09$ and $B = 0.06 \pm 0.09$ in Xu et al. (2019b), where $M_{\rm WD,derived}$ are derived with previous $I_{7.0}/I_{6.7}$–$M_{\rm WD}$ relations). For the combined Suzaku and XMM-Newton sample of 20 CVs, the best-fit yields $A = 0.90 \pm 0.15$, $B = 0.07 \pm 0.12$ and $r^2 = 0.93$. Both fittings are consistent with $A = 1$ and $B = 0$.

Besides, additional 20% systematic errors on non-robust mass measurements are also examined on above linear relation. The best-fit yields $A = 0.90 \pm 0.14$ and $B = 0.07 \pm 0.12$ that is the nearly same as above.[6] With the calibrated relations, we obtain the mean WD masses for IPs and DNe are $0.82 \pm 0.23\,M_{\odot}$ and $0.82 \pm 0.23\,M_{\odot}$, both of which are consistent with uncalibrated ones.

Finally, we compare the $M_{\rm WD}$ distribution with those from previous works. The comparison shows that our results are consistent with the those by Suleimanov et al. (2019), where $\langle M_{\rm WD}\rangle = 0.79 \pm 0.16\,M_{\odot}$ for IPs, and Zorotovic et al. (2011) where $\langle M_{\rm WD}\rangle = 0.83 \pm 0.23\,M_{\odot}$ for CVs.

4.2. Limitations

The results of this work suffer from several limitations, which are discussed as follows.

First, the typical uncertainties of $I_{7.0}/I_{6.7}$ in this work (∼20%–30%) are higher than those of Suzaku observed CVs (∼10%–20%, Xu et al. 2019b), which is presumably due to the limited counting statistics of XMM-Newton spectra in the Fe line energy ranges. For example, typical spectra of Suzaku observed CVs have more than 1000 bins between 5–8 keV, while those of XMM-Newton observed ones have about several hundred bins. In fact, XMM-Newton sources with better spectral quality do have better constrained $I_{7.0}/I_{6.7}$ values, e.g., the uncertainty is ∼9% for V426 Oph. Further observations on target CVs would improve the situation.

Second, the sample size is still not large enough, and could be biased toward luminous sources. Among the total 20 CVs (Figure 4) to derive the $I_{7.0}/I_{6.7}$–$M_{\rm WD}$ relations, there are nine new ones in this work and 11 old ones from previous works (Yu et al. 2018; Xu et al. 2019b). However, the sample size is certainly still not large enough, which should be dealt with in future works. Moreover, luminous sources would have higher chances to be selected as XMM-Newton targets and cause potential bias. We propose observations on less luminous ones (e.g., those with 2–10 keV luminosity below 10^{31} erg s^{-1}, which are supposed to have accretion rates below $10^{-11}\,M_{\odot}\,{\rm yr}^{-1}$) to test both the $I_{7.0}/I_{6.7}$–$M_{\rm WD}$ relations and their dependence on accretion rates in the future. Our sample is also lack of WDs more massive than $1.2M_{\odot}$, which should be improved by investigating the $I_{7.0}/I_{6.7}$ of CVs, especially DNe with massive WDs.

Third, the maximum WD mass derived from ipmass_line is $\sim 1.16\,M_{\odot}$ due to the hard limitations of apec description. $M_{\rm WD}$ of more massive WDs could not be derived with this method.

Fourth, the dynamical mass measurements used to calibrate the $I_{7.0}/I_{6.7}$–$M_{\rm WD}$ relations may not always be robust. For example, Marsh et al. (1987) and Hessman et al. (1989) suggested that a "hot spot" or the non-circular motions in the outer accretion disk may occur, which could distort the radial velocity curves and lead to biased $M_{\rm WD}$ measurements. Moreover, there are multiple measurements of WD masses in DNe, which are not always consistent with each other, thus could affect the best-fit of α in Equation (2). For example, we found $M_{\rm WD} = 0.81 \pm 0.19\,M_{\odot}$ (Bitner et al. 2007) and $M_{\rm WD} = 1.1 \pm 0.2\,M_{\odot}$ (Friend et al. 1990) for SS Cyg; $M_{\rm WD} = 0.89\,M_{\odot}$ (Mason et al. 2001) and $M_{\rm WD} = 0.5$–$0.6\,M_{\odot}$ (Matsumoto et al. 2000) for V893 Sco, and $M_{\rm WD} = 0.83 \pm 0.1\,M_{\odot}$ (Gilliland 1982) and $M_{\rm WD} = 1.24 \pm 0.22\,M_{\odot}$ (Watson et al. 2007) for BV Cen. To test the dependence of the $T_{\rm max}$–$M_{\rm WD}$ relation of DNe on these different measurements, we remove these sources from the sample, and refit Equation (2). The new best-fit yields $\alpha = 0.70 \pm 0.08$, which is still consistent with those of both the previous work (0.65 ± 0.07, Yu et al. 2018) and this work (0.69 ± 0.06).

Finally, we notice that EK TrA (Leftmost data point in Figure 2) seems to be more consistent with the $\alpha = 1$ curve

Table 5
Masses of WDs Derived from the ipmass_line or the dnmass_line Models and those Dynamically Measured for Suzaku Observed CVs

Source	Type	$M_{\rm WD}$[a] ($M_{\odot}$)	χ^2_{ν}(d.o.f.)	$M_{\rm WD}$[b] ($M_{\odot}$)
VW Hyi	DN	$0.65^{+0.08}_{-0.04}$	1.10(172)	0.67 ± 0.22
V1159 Ori	DN	$0.50^{+0.23}_{-0.23}$	0.84(190)	⋯
FS Aur	DN	$0.84^{+0.33}_{-0.30}$	0.80(228)	⋯
SS Aur	DN	$0.93^{+0.23}_{-0.20}$	0.85(104)	1.08 ± 0.4
U Gem	DN	$1.13^{+0.09}_{-0.09}$	0.90(871)	1.2 ± 0.05
BZ UMa	DN	$0.75^{+0.22}_{-0.22}$	0.99(98)	0.65 ± 0.15
CH UMa	DN	$0.79^{+0.12}_{-0.11}$	0.84(214)	⋯
BV Cen	DN	$1.00^{+0.10}_{-0.10}$	0.96(705)	1.24 ± 0.22
EK TrA	DN	$0.55^{+0.09}_{-0.10}$	1.07(280)	0.46 ± 0.1
V893 Sco	DN	$0.83^{+0.04}_{-0.07}$	0.76(697)	0.89 ± 0.15
SS Cyg	DN	$1.18^{+0.06}_{-0.07}$	0.93(1481)	1.1 ± 0.2
V709 Cas	IP	$1.14^{+0.26}_{-0.38}$	0.91(1813)	⋯
XY Ari	IP	$0.91^{+0.49}_{-0.27}$	0.98(626)	1.04 ± 0.13
TV Col	IP	$0.64^{+0.12}_{-0.09}$	0.98(1970)	0.75 ± 0.15
TX Col	IP	$0.66^{+0.24}_{-0.14}$	0.87(949)	⋯
MU Cam	IP	$1.09^{+0.31}_{-0.29}$	0.87(880)	⋯
BG CMi	IP	$0.79^{+0.61}_{-0.40}$	0.98(389)	0.8 ± 0.2
PQ Gem	IP	$0.82^{+0.58}_{-0.32}$	0.96(1327)	⋯
YY Dra	IP	$0.73^{+0.20}_{-0.12}$	0.98(1183)	0.83 ± 0.1
NY Lup	IP	$0.82^{+0.14}_{-0.09}$	0.98(2241)	⋯
V2400 Oph	IP	$0.75^{+0.10}_{-0.09}$	1.05(2429)	⋯
CXOU J171935.8-410053	IP	$1.08^{+0.32}_{-0.24}$	0.89(1596)	⋯
V1223 Sgr	IP	$0.92^{+0.15}_{-0.12}$	1.05(2428)	⋯
RX J2133.7+5107	IP	$0.97^{+0.43}_{-0.22}$	0.96(1911)	⋯
FO Aqr	IP	$0.52^{+0.14}_{-0.13}$	0.97(2023)	⋯
AO Psc	IP	$0.51^{+0.07}_{-0.06}$	0.96(1975)	⋯

Notes.
[a] WD masses derived with the ipmass_line (or the dnmass_line) model for Suzaku observed CVs.
[b] WD masses from dynamical measurements.

[6] All errors in linear relation are shown with 90% confidence level.

Table 6
Masses of WDs Derived from ipmass_line or dnmass_line Model and those Dynamically Measured for XMM-Newton Observed CVs

Source	Type	M_{WD}[a]	χ^2_ν(d.o.f.)	M_{WD}[b]	M_{WD}[a]
		($M_\odot$)		($M_\odot$)	($M_\odot$)
WW Cet	DN	$0.70^{+0.17}_{-0.22}$	0.95(250)	0.83 ± 0.16	⋯
HT Cas	DN	$0.71^{+0.14}_{-0.12}$	0.97(235)	0.61 ± 0.04	⋯
VW Hyi	DN	$0.71^{+0.11}_{-0.10}$	0.92(133)	0.67 ± 0.22	$0.65^{+0.08}_{-0.04}$
SS Aur	DN	$1.00^{+0.28}_{-0.18}$	1.02(113)	1.08 ± 0.4	$0.93^{+0.23}_{-0.20}$
U Gem	DN	$1.08^{+0.13}_{-0.12}$	0.81(380)	1.2 ± 0.05	$1.13^{+0.09}_{-0.09}$
Z Cha	DN	$0.69^{+0.07}_{-0.11}$	1.00(657)	0.84 ± 0.09	⋯
YZ Cnc	DN	$0.84^{+0.08}_{-0.07}$	1.00(318)	0.82 ± 0.08	⋯
SU UMa	DN	$1.10^{+0.27}_{-0.27}$	0.84(141)	⋯	⋯
OY Car	DN	$0.66^{+0.05}_{-0.05}$	0.88(466)	0.685 ± 0.011	⋯
QZ Vir	DN	$0.54^{+0.11}_{-0.14}$	1.06(184)	0.375 ± 0.025	⋯
V1129 Cen	DN	$0.66^{+0.29}_{-0.21}$	1.01(136)	⋯	⋯
V893 Sco	DN	$0.74^{+0.05}_{-0.05}$	1.08(855)	0.89 ± 0.15	$0.83^{+0.04}_{-0.07}$
V426 Oph	DN	$1.03^{+0.06}_{-0.05}$	0.97(891)	0.9 ± 0.19	⋯
SS Cyg	DN	$1.12^{+0.14}_{-0.13}$	1.03(785)	1.1 ± 0.2	$1.18^{+0.06}_{-0.07}$
RU Peg	DN	$1.13^{+0.10}_{-0.08}$	0.98(880)	1.06 ± 0.04	⋯
V405 Peg	DN	$0.63^{+0.15}_{-0.13}$	1.06(78)	⋯	⋯
V1033 Cas	IP	$0.66^{+0.46}_{-0.25}$	0.93(422)	⋯	⋯
V709 Cas	IP	$1.16^{+0.24}_{-0.22}$	1.07(885)	⋯	$1.14^{+0.26}_{-0.38}$
V515 And	IP	$0.90^{+0.26}_{-0.23}$	0.91(746)	⋯	⋯
XY Ari	IP	$1.16^{+0.24}_{-0.51}$	0.91(408)	1.04 ± 0.13	$0.91^{+0.49}_{-0.27}$
2MASS J04570832+4527499	IP	$1.16^{+0.24}_{-0.48}$	0.93(657)	⋯	⋯
RX J0525.3+2413	IP	$1.09^{+0.31}_{-0.84}$	0.98(394)	⋯	
MU Cam	IP	$0.86^{+0.54}_{-0.66}$	0.73(99)	⋯	$1.09^{+0.31}_{-0.29}$
V647 Aur	IP	$0.96^{+0.44}_{-0.60}$	0.85(246)	⋯	⋯
PQ Gem	IP	$0.69^{+0.71}_{-0.24}$	0.86(847)	⋯	$0.82^{+0.58}_{-0.32}$
HT Cam	IP	$0.89^{+0.51}_{-0.37}$	0.95(140)	⋯	⋯
DW Cnc	IP	$0.62^{+0.39}_{-0.19}$	0.86(234)	⋯	⋯
EI UMa	IP	$0.64^{+0.36}_{-0.20}$	0.93(523)	⋯	⋯
Swift J0927.7-6945	IP	$0.98^{+0.42}_{-0.34}$	1.15(290)	⋯	
V1025 Cen	IP	$0.48^{+0.18}_{-0.11}$	1.01(272)	⋯	⋯
VVV J140845.99-610754.1	IP	$0.65^{+0.75}_{-0.24}$	1.13(105)	⋯	
2MASS J15092601-6649232	IP	$0.74^{+0.66}_{-0.24}$	1.01(798)	⋯	⋯
NY Lup	IP	$0.96^{+0.44}_{-0.22}$	0.98(870)	⋯	$0.82^{+0.14}_{-0.09}$
2MASS J16495517-3307088	IP	$1.16^{+0.24}_{-0.31}$	0.85(625)	⋯	⋯
Swift J1701.3-4304	IP	$1.01^{+0.39}_{-0.39}$	0.89(354)	⋯	
V2400 Oph	IP	$1.16^{+0.24}_{-0.54}$	0.95(508)	⋯	$0.75^{+0.10}_{-0.09}$
CXOU J171935.8-410053	IP	$1.10^{+0.30}_{-0.34}$	1.00(913)	⋯	$1.08^{+0.32}_{-0.24}$
2MASS J18043892-1456474	IP	$0.91^{+0.49}_{-0.28}$	0.97(275)	⋯	⋯
IGR J18173-2509	IP	$0.38^{+0.22}_{-0.17}$	0.98(806)	⋯	⋯
IGR J18308-1232	IP	$0.76^{+0.36}_{-0.22}$	0.97(497)	⋯	⋯
AX J1832.3-0840	IP	$0.82^{+0.30}_{-0.22}$	0.92(579)	⋯	⋯
XMMU J185330.7-012815	IP	$0.53^{+0.25}_{-0.16}$	0.90(184)	⋯	⋯
V1223 Sgr	IP	$0.93^{+0.19}_{-0.19}$	1.10(980)	⋯	$0.92^{+0.15}_{-0.12}$
1RXS J211336.1+542226	IP	$0.76^{+0.33}_{-0.17}$	0.91(353)	⋯	
V2069 Cyg	IP	$0.76^{+0.64}_{-0.37}$	0.86(439)	⋯	⋯
RX J2133.7+5107	IP	$1.11^{+0.29}_{-0.68}$	0.95(681)	⋯	$0.97^{+0.43}_{-0.22}$
FO Aqr	IP	$0.72^{+0.40}_{-0.23}$	0.96(959)	⋯	$0.52^{+0.14}_{-0.13}$
AO Psc	IP	$0.48^{+0.06}_{-0.05}$	0.96(980)	⋯	$0.51^{+0.07}_{-0.06}$

Notes.
[a] Derived WD masses with ipmass_line (or dnmass_line) model for XMM-Newton and Suzaku, respectively.
[b] WD masses from dynamical measurements.

than the $\alpha = 0.69$ curve in Figure 2. It may attribute to possible uncertainties of previous mass measurements, or to other physical reasons (e.g., the change of accretion pattern and the boundary layer for CVs with orbital periods below 2 h). Therefore, we still keep α as the only parameter for the T_{max} –M_{WD} relation in this work. Further mass measurements would be necessary to distinguish whether EK TrA is a true outlier.

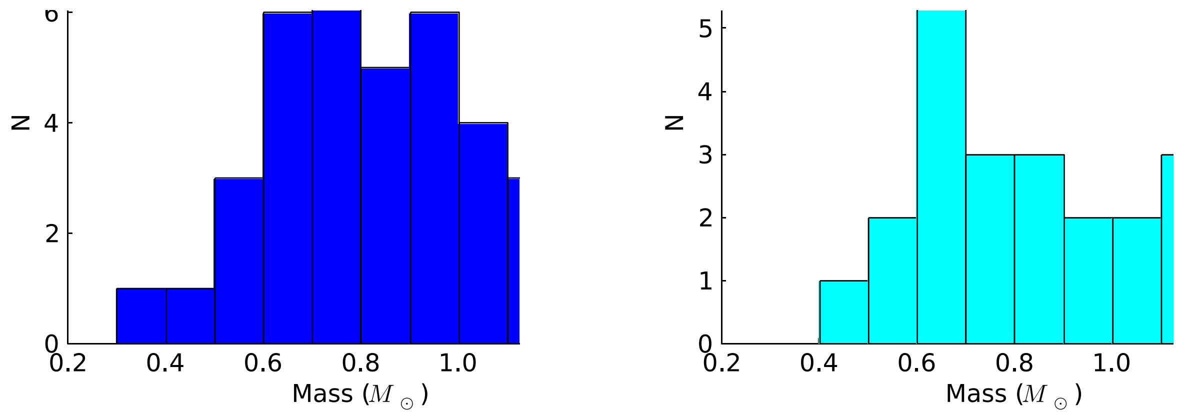

Figure 5. Masses of WDs derived from the ipmass_line and the dnmass_line models for sampled IPs (left panel) and DNe (right panel).

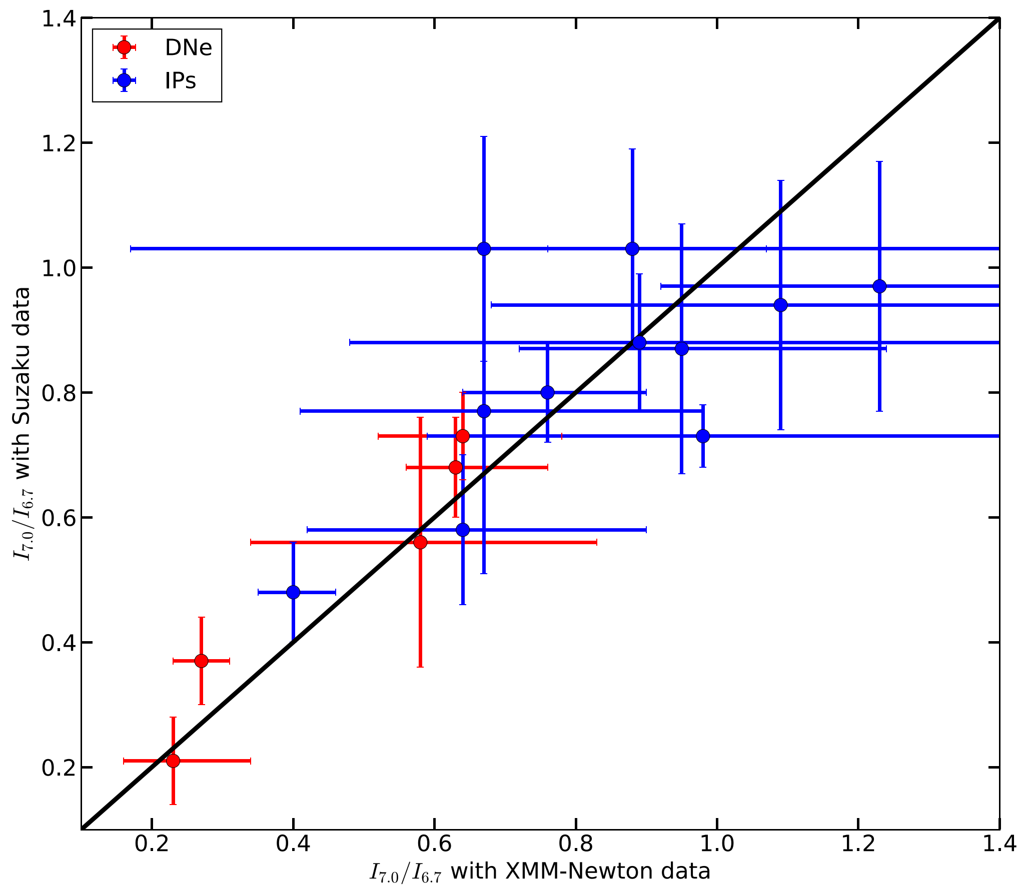

Figure 6. $I_{7.0}/I_{6.7}$ measured with XMM-Newton data in this work versus those measured with Suzaku data by Xu et al. (2016). The black solid diagonal line shows a 1:1 relation of the $I_{7.0}/I_{6.7}$ values.

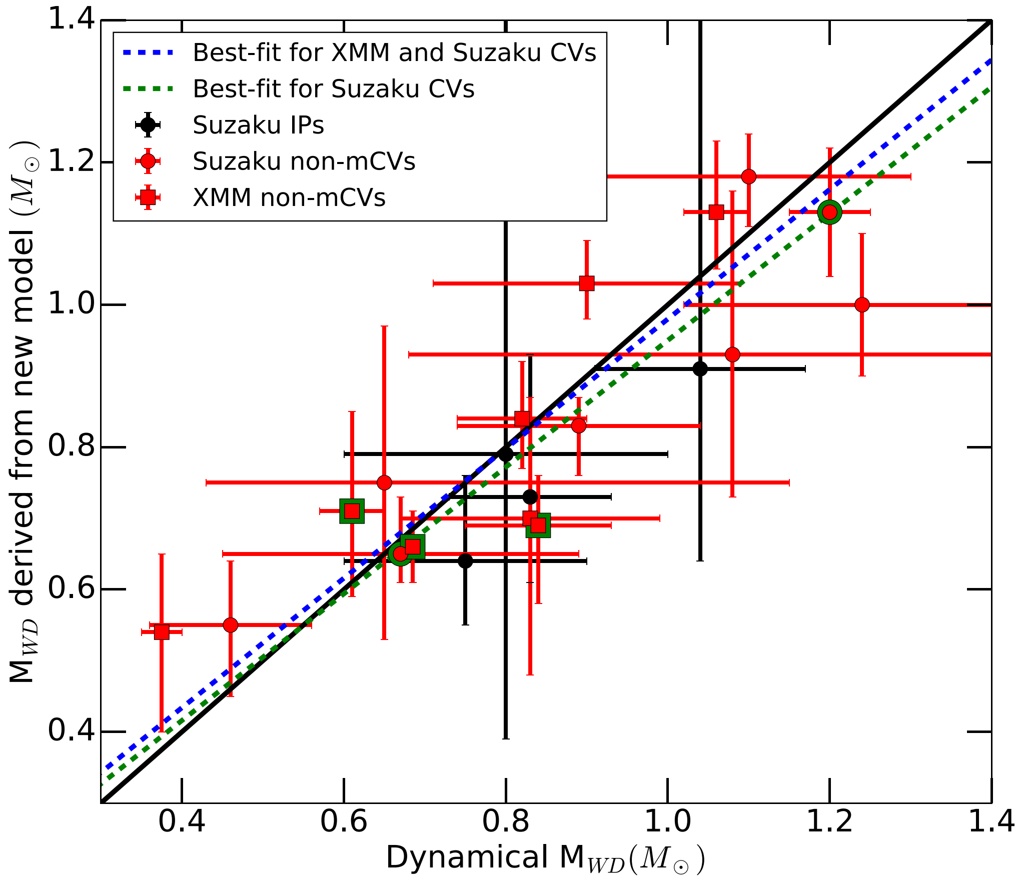

Figure 7. $M_{\rm WD}$ derived from the ipmass_line or the dnmass_line models versus dynamically determined ones. The black (red) data points represent IPs (non-mCVs), the squares and dots represent CVs observed with XMM-Newton and Suzaku in this work, respectively. The solid diagonal line shows a 1:1 relation for the $M_{\rm WD}$ values. The blue dashed line shows the best linear fit to all CVs, and the green dashed line for Suzaku observed CVs only. Points surrounded by green represent CVs from Zorotovic et al. (2011)'s fiducial sub-sample of "robust dynamical mass measurements".

5. Summary

In this work we carry out a systematic investigation on the WD masses of 58 CVs (including 36 IPs and 22 DNe) observed by XMM-Newton and Suzaku in the solar vicinity based on the $I_{7.0}/I_{6.7}$–$T_{\rm max}$–$M_{\rm WD}$ relations using the mkcflow model with apec description and AtomDB. Our main results are summarized as follows:

1. The $T_{\rm max}$ –$M_{\rm WD}$ relation $\left(T_{\rm max}, =, \alpha, \frac{3}{16}, \frac{\mu m_{\rm H}}{k}, \frac{GM_{\rm WD}}{R_{\rm WD}}\right)$ for DNe is examined with the mkcflow model with the apec description. The results yield $\alpha = 0.69 \pm 0.06$, which is consistent with previous works.

2. The $I_{7.0}/I_{6.7}$, $M_{\rm WD}$ and $T_{\rm max}$ of sampled CVs follow the theoretical (semi-empirical for DNe) relations predicted by the mkcflow model with the apec description.

3. We introduce a new spectral model to measure $M_{\rm WD}$ by building the $I_{7.0}/I_{6.7}$–$T_{\rm max}$–$M_{\rm WD}$ relations into the mkcflow model with the apec description. With constraints on the metallicity Z, the fitting of the 5–8 keV spectra of CVs with this model can output $M_{\rm WD}$ directly.

4. Based on the above model, we derive the WD masses of IPs and DNe in the largest X-ray selected sample. The mean WD masses are $\langle M_{\rm WD,IP}\rangle = 0.81 \pm 0.21\, M_\odot$ and $\langle M_{\rm WD,DN}\rangle = 0.81 \pm 0.21\, M_\odot$ for IPs and DNe, respectively. We also do not find significant difference between the two WD mass distributions. These values are consistent with the optical and hard X-ray measurements of WD masses in CVs in the solar vicinity.

Acknowledgments

We thank the anonymous referee for the very useful comments and suggestions which helped to improve this paper greatly. This work is supported by the National Natural Science Foundation of China through Grant 11873029 and the National Key Research and Development Program of China (2016YFA0400803 and 2017YFA0402703). This work is based on observations obtained with XMM-Newton, an ESA science mission with instruments and contributions directly funded by ESA Member States and NASA.

References

Bernardini, F., de Martino, D., Falanga, M., et al. 2012, A&A, 542, A22
Beuermann, K., & Reinsch, K. 2008, A&A, 480, 199
Bitner, M. A., Robinson, E. L., & Behr, B. B. 2007, ApJ, 662, 564
Briggs, G. P., Ferrario, L., Tout, C. A., & Wickramasinghe, D. T. 2018, MNRAS, 481, 3604
Byckling, K., Mukai, K., Thorstensen, J. R., & Osborne, J. P. 2010, MNRAS, 408, 2298
de Martino, D., Bernardini, F., Mukai, K., Falanga, M., & Masetti, N. 2020, AdSpR, 66, 1209
Dunford, A., Watson, C. A., & Smith, R. C. 2012, MNRAS, 422, 3444
Ezuka, H., & Ishida, M. 1999, ApJS, 120, 277
Fertig, D., Mukai, K., Nelson, T., & Cannizzo, J. K. 2011, PASP, 123, 1054
Frank, J., King, A., & Raine, D. J. 2002, Accretion Power in Astrophysics (3rd edn; Cambridge: Cambridge Univ. Press)
Friend, M. T., Martin, J. S., Smith, R. C., & Jones, D. H. P. 1990, MNRAS, 246, 654
Gänsicke, B. T., Beuermann, K., & Thomas, H. C. 1997, MNRAS, 289, 388
Gilliland, R. L. 1982, ApJ, 263, 302
Hailey, C. J., Mori, K., Perez, K., et al. 2016, ApJ, 826, 160
Hamilton, R. T., Harrison, T. E., Tappert, C., & Howell, S. B. 2011, ApJ, 728, 16
Haswell, C. A., Patterson, J., Thorstensen, J. R., Hellier, C., & Skillman, D. R. 1997, ApJ, 476, 847
Hellier, C. 1993, MNRAS, 264, 132
Hellier, C. 1997, MNRAS, 291, 71
Hessman, F. V. 1988, A&AS, 72, 515
Hessman, F. V., Koester, D., Schoembs, R., & Barwig, H. 1989, A&A, 213, 167
Horne, K., Wood, J. H., & Stiening, R. F. 1991, ApJ, 378, 271
Jurcevic, J. S., Honeycutt, R. K., Schlegel, E. M., & Webbink, R. F. 1994, PASP, 106, 481
Kepler, S. O., Kleinman, S. J., Nitta, A., et al. 2007, MNRAS, 375, 1315
Knigge, C. 2006, MNRAS, 373, 484
Knigge, C., Baraffe, I., & Patterson, J. 2011, ApJS, 194, 28
Marsh, T. R., Horne, K., & Shipman, H. L. 1987, MNRAS, 225, 551
Mason, E., Skidmore, W., Howell, S. B., & Mennickent, R. E. 2001, ApJ, 563, 351
Matsumoto, K., Mennickent, R. E., & Kato, T. 2000, A&A, 363, 1029
Mukai, K. 2017, PASP, 129, 062001
Mukai, K., Rana, V., Bernardini, F., & de Martino, D. 2015, ApJL, 807, L30
Mushotzky, R. F., & Szymkowiak, A. E. 1988, in NATO Advanced Study Institute (ASI) Series C, Vol. 229, Cooling Flows in Clusters and Galaxies, ed. A. C. Fabian, 53
Nauenberg, M. 1972, ApJ, 175, 417
Nobukawa, M., Uchiyama, H., Nobukawa, K. K., Yamauchi, S., & Koyama, K. 2016, ApJ, 833, 268
Penning, W. R. 1985, ApJ, 289, 300
Rana, V. R., Singh, K. P., Schlegel, E. M., & Barrett, P. E. 2006, ApJ, 642, 1042
Ritter, H., & Kolb, U. 2003, A&A, 404, 301
Shafter, A. W., & Hessman, F. V. 1988, AJ, 95, 178
Shafter, A. W., & Szkody, P. 1984, ApJ, 276, 305
Shaw, A. W., Heinke, C. O., Mukai, K., et al. 2018, MNRAS, 476, 554
Shaw, A. W., Heinke, C. O., Mukai, K., et al. 2020, MNRAS, 498, 3457
Sion, E. M., Gänsicke, B. T., Long, K. S., et al. 2008, ApJ, 681, 543
Suleimanov, V., Doroshenko, V., Ducci, L., Zhukov, G. V., & Werner, K. 2016, A&A, 591, A35
Suleimanov, V. F., Doroshenko, V., & Werner, K. 2019, MNRAS, 482, 3622
Wade, R. A., & Horne, K. 1988, ApJ, 324, 411
Watson, C. A., Steeghs, D., Shahbaz, T., & Dhillon, V. S. 2007, MNRAS, 382, 1105
Wood, J. H., Horne, K., Berriman, G., & Wade, R. A. 1989, ApJ, 341, 974
Xu, X.-j., Li, Z., Zhu, Z., et al. 2019a, ApJ, 882, 164
Xu, X.-j., Wang, Q. D., & Li, X.-D. 2016, ApJ, 818, 136
Xu, X.-j., Yu, Z.-l., & Li, X.-d 2019b, ApJ, 878, 53
Yu, Z.-l., Xu, X.-j., Li, X.-D., et al. 2018, ApJ, 853, 182
Yuasa, T., Nakazawa, K., Makishima, K., et al. 2010, A&A, 520, A25
Zhu, Z., Li, Z., & Morris, M. R. 2018, ApJS, 235, 26
Zorotovic, M., & Schreiber, M. R. 2020, AdSpR, 66, 1080
Zorotovic, M., Schreiber, M. R., & Gänsicke, B. T. 2011, A&A, 536, A42